Springer

Journal of
Mechanical
Science and
Technology

Journal of Mechanical Science and Technology 22 (2008) 2542~2553

www.springerlink.com/content/1738-494x
DOI 10.1007/s12206-008-0816-8

Numerical simulation of fluid-structure interaction of a moving flexible foil †

Sangmook Shin[1,*] and Hyoung Tae Kim[2]

[1]*Department of Naval Architecture and Marine Systems Engineering, Pukyong National University, Busan, 608-737, Korea*
[2]*Department of Naval Architecture and Ocean Engineering, Chungnam National University, Daejeon, 305-764, Korea*

(Manuscript Received September 20, 2007; Revised August 13, 2008; Accepted August 14, 2008)

Abstract

The hybrid Cartesian/immersed boundary method is applied to fluid-structure interaction of a moving flexible foil. A new algorithm is suggested to classify immersed boundary nodes based on edges crossing a boundary. Velocity vectors are reconstructed at the immersed boundary nodes by using the interpolation along a local normal line to the boundary. For eliminating pressure reconstruction, the hybrid staggered/non-staggered grid method is adapted. The deformation of an elastic body is modeled based on dynamic thin-plate theory. To validate the developed code first, free rotation of a foil in a channel flow is simulated and the computed angular motion is compared with other computational results. The code is then applied to the fluid-structure interaction of a moving flexible foil which undergoes large deformation due to the fluid loading caused by horizontal sinusoidal motion. It has been shown that the moving flexible foil can generate much larger vertical force than the corresponding rigid foil and the vertical force can be attributed to the downward fluid jet due to the alternating tail deflection.

Keywords: Dynamic thin-plate theory; Fluid-structure interaction; Hybrid Cartesian/immersed boundary method; Hybrid staggered/non-staggered grid

1. Introduction

There is growing interest of the dynamic interaction of a flexible body with a neighboring fluid. For many applications, a soft material is used because of its required mechanical properties such as low density, durability or high acoustic damping. However, the flexibility of a body may also improve its performance according to circumstances. For the micro-aviation vehicle (MAV), it was reported that the flexibility of a flapping foil increases its aerodynamic efficiency [1-2].

In point of view of computational fluid dynamics, the main difficulty of the dynamic fluid-structure interaction is related to the continual deformation of a fluid domain. Although many researchers have suggested a wide variety of numerical schemes to handle the deforming boundary, the problem is still challenging. The numerical schemes to treat the deforming boundary can be categorized into two classes: boundary conforming and non-boundary conforming. The arbitrary Lagrangian-Eulerian method is a typical example of the boundary conforming method [3-4]. Since the grid is always adapted to an instantaneous boundary, the clustering of a grid can be controlled to resolve the variation of dependent variables within a boundary layer. However, the quality of the deforming grid may cause difficulties for arbitrarily large deformations. In addition, the tiny irregularity introduced in the deforming boundary may cause more severe problems when numerical cells of high aspect ratio are used near the body boundary.

Due to their inherent versatility, the non-boundary conforming methods attract increasing attention in

† This paper was recommended for publication in revised form by Associate Editor Haecheon Choi

* Corresponding author. Tel.: +82 51 629 6617, Fax.: +82 51 629 6608
E-mail address: smshin@pknu.ac.kr

connection with a complicated boundary. Many researchers adapted the immersed boundary method to handle deforming or moving boundaries [5-7]. For the immersed boundary method, the smoothed delta function is introduced to distribute the forcing over a few cells near the body boundary. This forcing distribution increases the spatial resolution requirements according to the configuration of the boundary, for instance a trailing edge of a foil. To maintain a sharp interface, several methods have been developed including the immersed interface method [8] and the Cartesian method [9].

Recently, Sotiropoulos and his co-workers suggested the hybrid Cartesian/immersed boundary method [10-12]. This method can handle arbitrarily large deformations of a zero-thickness body. In this method, the immersed boundary nodes are distributed inside of a fluid domain and velocity vectors are reconstructed at those immersed boundary nodes to provide boundary conditions for the discretized flow problem. To eliminate pressure reconstruction at the immersed boundary nodes, the hybrid staggered/non-staggered grid method has been suggested. Shin et al. [13] suggested a new criterion to classify the nodes so that the velocity reconstruction at the immersed boundary nodes makes the discretized flow problem well-posed for the solver based on the hybrid staggered/non-staggered grid.

In this study, the hybrid Cartesian/immersed boundary method is expanded to the fluid-structure interaction where dynamic deformation of an elastic body should be calculated based on the fluid loading caused by arbitrary body motion. A procedure is suggested to conclude the node classification without any checking algorithm for nodes outside of a fluid domain. In section 2, the details of the flow solver based on the hybrid staggered/non-staggered grid are explained. For the validation of the developed code, the motion of a foil which is free to rotate about a fixed point in a channel flow is simulated and the present results are compared with other computations in section 3. The code is applied to the fluid-structure interaction of a moving flexible foil in section 4. In section 5, the concluding remarks are provided.

2. Flow solver using the hybrid Cartesian/immersed boundary method

The governing equations are the incompressible unsteady Navier-Stokes equations. The deforming interface is discretized by a set of the Lagrangian control points distributed on the boundary. The position and velocity vectors at the Lagrangian control points provide the boundary conditions for the flow solver. The hybrid Cartesian/immersed boundary method is used based on the hybrid staggered/non-staggered grid so that the boundary condition for the pressure is not required explicitly. For the incompressibility condition, the artificial compressibility is introduced with respect to the pseudotime.

2.1 Categorization of nodes based on the edges crossing a boundary

In the hybrid Cartesian/immersed boundary method, the velocity vectors are reconstructed at the immersed boundary nodes which are distributed inside of a fluid domain near an interface. The distribution of immersed boundary nodes should be appropriate to ensure that the reconstruction of velocity vectors at the immersed boundary nodes makes the discretized problem well-posed. In this study, a node is categorized as an immersed boundary node if the node is included in the fluid domain and it is connected to an edge crossing the boundary. If a node is not an immersed boundary node and it is inside of the fluid domain, then the node is classified as a fluid node. This criterion guarantees there is no fluid node connected to a solid node which is outside of the fluid domain. This property is important to avoid using dependent variables which are not stored near the boundary as explained later.

Gilmanov et al. [10] suggested identifying a node as an immersed boundary node if the node is inside of a fluid domain and it is connected to a solid node. This original criterion guarantees that no fluid node is connected to a solid node by an edge. However, this criterion cannot handle a thin body. Gilmanov and Sotiropoulos [11] modified the criterion so that the immersed boundary nodes are identified based on the distances from the boundary. Even though the modified criterion can be applicable to a zero-thickness body, there is an ambiguity in the distance margin to guarantee that no fluid node is connected to a solid node, especially for the case where the grid spacing is varied along the boundary. The present criterion can handle a zero-thickness body without any additional treatment because the edges crossing a boundary can be identified clearly regardless of thickness of a body. In addition, it is guaranteed by the criterion for the

immersed boundary node that there is no fluid node connected to a solid node by an edge.

Fig. 1 shows an example of identified immersed boundary nodes based on the present criterion. Using the present criterion, the categorization of nodes can be concluded without any checking procedure about whether a node is included in a fluid domain or not. Initially, every node is assumed as a fluid node. For each line segment connecting two neighboring Lagrangian control points, all edges of a background Cartesian grid are checked regarding whether they cross the given line segment. If an edge crosses the line segment on the boundary, two nodes of the edge are inspected. According to the normal vector of the line segment, each node should be classified as an immersed boundary node or a solid node. However, for the case where the node is presumed to be a solid node based on the given line segment, it should be checked whether the node has been identified already as an immersed boundary node based on other line segments. If the node is identified as an immersed boundary node based on one line segment and at the same time it is presumed to be a solid node based on other line segment, it implies that the thickness of the body is less than the local grid spacing and the node should be an immersed boundary node. Finally, the categorization procedure is concluded by identifying additional solid node, which is not changed from a fluid node to a solid node but it is connected to a solid node by an edge.

2.2 Velocity reconstruction at an immersed boundary node

The essential idea of the hybrid Cartesian/immersed boundary method is the reconstruction of a velocity vector at an immersed boundary node based on the interpolation along a local normal line to a boundary. Fig. 2 shows the velocity reconstruction at immersed boundary nodes near a sharp corner. For every immersed boundary node, a line is assigned that passes the given immersed boundary node IB_j and intersects the boundary at S_j orthogonally. If the orthogonal line cannot be defined for the given immersed boundary node due to a sharp convex corner, then a line connecting the given immersed boundary node and the closest point on the boundary replaces the orthogonal line. Once the interpolation direction is selected, the line is extended from the immersed boundary node IB_j to a point E_j on an internal edge of the background Cartesian grid.

At the point S_j on the boundary, the velocity vector is determined based on the velocity vectors prescribed at two neighboring Lagrangian control points at given physical time step. At the other end point E_j of the interpolation line, the velocity vector is estimated based on the intermediate velocity vectors at both nodes of the edge, N_{1j} and N_{2j} which are updated during the pseudotime iteration for the incompressibility condition. In this study, a linear variation of the velocity vector along the internal edge is assumed:

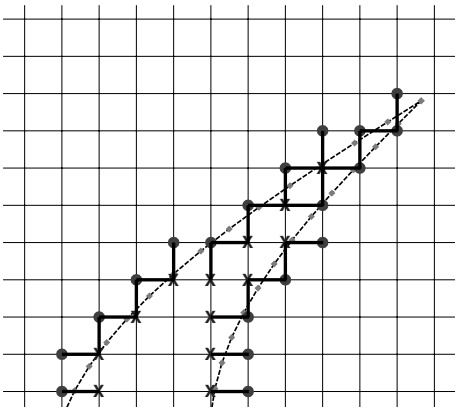

Fig. 1. Node classification based on edges crossing the boundary. Lagrangian control points, diamonds; immersed boundary nodes, circles; solid nodes, crosses.

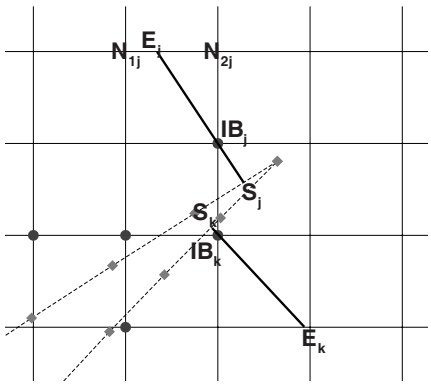

Fig. 2. Velocity reconstruction at an immersed boundary node based on the interpolation along a local normal line to the boundary.

$$\phi_{E_j}{}^{l} = \frac{1}{d_{N_{1j}-E_j} + d_{N_{2j}-E_j}} \left(d_{N_{2j}-E_j} \phi_{N_1}^{l} + d_{N_{1j}-E_j} \phi_{N_2}{}^{l} \right) \tag{1}$$

where $\phi_{E_j}{}^{l}$ is the estimated velocity component at the end point E_j of the interpolation line at the l th pseudotime step, $d_{N_{1j}-E_j}$ is the distance from the node N_{1j} to the point E_j and $\phi_{N_{1j}}{}^{l}$ is the intermediate velocity component at the node N_{1j} during the pseudotime iteration. The velocity components at given immersed boundary node are estimated based on the distances from the immersed boundary node IB_j to the end points S_j and E_j of the interpolation line. In this study a linear variation of the velocity vector is assumed near the immersed boundary node along the interpolation line:

$$\phi_{IB_j}{}^{l} = \frac{1}{d_{IB_j-E_j} + d_{IB_j-S_j}} \left(d_{IB_j-E_j} \phi_{S_j} + d_{IB_j-S_j} \phi_{E_j}{}^{l} \right) \tag{2}$$

In Eq. (2), the velocity vector is unchanged at the point S_j on the boundary during one physical time step, but the velocity vector reconstructed at the immersed boundary node should be updated as the pseudotime iteration marches according to the updated velocity vector at the point E_j on the internal edge.

2.3 Incompressible flow solver based on the hybrid staggered/non-staggered grid

The use of the non-staggered grid makes the velocity reconstruction procedure simple. However, pressure is required at the immersed boundary node for the flow solver based on the non-staggered grid. Compared with the reconstruction of velocity, the reconstruction of pressure at the immersed boundary node may cause difficulties. Near the deforming boundary, the pressure field of the incompressible flow may change abruptly. In addition, only the approximation of normal derivative of pressure is available on the boundary, whereas the Dirichlet-type boundary condition is specified for the velocity field. Although additional interpolations are required between dependent variables of the two grids, the hybrid staggered/non-staggered grid method provides important advantages resulting from eliminating the reconstruction of pressure at the immersed boundary nodes in the hybrid Cartesian/immersed boundary method.

Fig. 3 shows the arrangement of dependent variables for the hybrid staggered/non-staggered grid method near a sharp body end. At the immersed boundary nodes (open circles), the non-staggered velocity components are reconstructed. For the fluid nodes (filled circles), the pressure and non-staggered velocity components are stored. At a mid-point of an edge connecting an immersed boundary node and a fluid node (open triangle), the staggered velocity component in the direction of the edge is interpolated based on the velocity components of the two nodes. At a mid-point of an edge connecting two fluid nodes (filled triangle), the staggered velocity component is stored.

At every fluid node, the convection and diffusion terms of x - and y -momentum equations are computed. The convection term is discretized based on the second-order upwind biased scheme. For the case where the velocity component at a solid node is required, the second-order scheme is replaced with the first-order upwind scheme to reduce the stencil. However, Gilmanov et al. [10] showed that this approximation near the boundary does not degrade the second-order accuracy of the scheme in space based on the error behavior with respect to grid spacing in the log-log plot. To explain this behavior, it is pointed out that the truncation error of the first-order upwind scheme is proportional to the second-order spatial derivative and the linear variation of the velocity is assumed near an immersed boundary node. It can be easily confirmed that the convection and diffusion terms can be calculated at every fluid node based on well-defined velocity vectors, provided that there is no fluid node which is connected to a solid node by

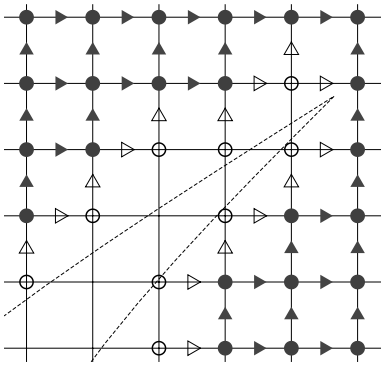

Fig. 3. Arrangement of the dependent variables for the hybrid staggered/non-staggered grid method near the boundary.

an edge.

To calculate the staggered velocity components at mid-points of edges connecting two fluid nodes (filled triangles), the sums of convection and diffusion terms are interpolated based on those at two fluid nodes of the edges:

$$XCD^{l}_{i+1/2,j} = \frac{1}{2}\left(XCD^{l}_{i,j} + XCD^{l}_{i+1,j} \right) \tag{3}$$

$$YCD^{l}_{i,j+1/2} = \frac{1}{2}\left(YCD^{l}_{i,j} + YCD^{l}_{i,j+1} \right) \tag{4}$$

where XCD and YCD are the sums of the convection and diffusion terms of the x - and y - momentum equations, respectively. The pressure gradient is calculated based on the pressure at two fluid nodes of the edge.

To satisfy the incompressibility condition, the artificial compressibility is introduced with respect to the pseudotime within every physical time step:

$$\frac{p^{n+1,l+1}_{i,j} - p^{n+1,l}_{i,j}}{\Delta\tau} + \beta\left(\frac{u^{n+1,l}_{i+1/2,j} - u^{n+1,l}_{i-1/2,j}}{\Delta x} + \frac{v^{n+1,l}_{i,j+1/2} - v^{n+1,l}_{i,j-1/2}}{\Delta y} \right) = 0 \tag{5}$$

where β is the artificial compressibility parameter and $\Delta\tau$ is the pseudotime step size. The superscript $(n+1, l)$ indicates the l th pseudotime iteration within the $(n+1)$th physical time step. For the physical time marching, the three-point second-order backward difference formula is used:

$$\frac{u^{n+1,l+1}_{i+1/2,j} - u^{n+1,l}_{i+1/2,j}}{\Delta\tau} + \frac{3u^{n+1,l+1}_{i+1/2,j} - 4u^{n}_{i+1/2,j} + u^{n-1}_{i+1/2,j}}{2\Delta t} + XCD^{n+1,l}_{i+1/2,j} + \frac{p^{n+1,l}_{i+1,j} - p^{n+1,l}_{i,j}}{\Delta x} = 0 \tag{6}$$

After the staggered velocity components are computed at mid-points of the edges connecting two fluid nodes, the non-staggered velocity components at the fluid nodes are interpolated based on the neighboring staggered velocity components. For every physical time step, the position and velocity vectors of the Lagrangian control points are updated. Based on the updated position vectors of the Lagrangian control points, the nodes are categorized and the interpolation lines for the immersed boundary nodes are updated. To avoid the use of undefined dependent variables, there should be no node that is converted from a solid node to a fluid node within one physical time step. The physical time step size Δt should be restricted so that the interface never seeps for a whole cell within one physical time step.

3. Free rotation of a NACA0012 in a channel flow

The developed code is applied to simulate the rotational motion of an NACA0012 in a channel flow. In this example, the foil is rigid and free to rotate around a fixed point due to a viscous flow. Wan and Turek [14] and Glowinski et al. [15, 16] reported the computational results of this problem. Fig. 4 shows a schematic drawing for this computation. The fluid domain is $-4 \le x \le 16$ and $-2 \le y \le 2$ and the chord length of the foil is 1.009. The fixed point is located at (0.42,0). The density ratio of the foil to the fluid is 1.1. At x =-4, the uniform inflow is given and the no-slip condition is used at $y = \pm 2$ and on the body boundary. The flow starts from the rest and both the angle θ and the angular velocity $d\theta/dt$ of the foil are zero at t =0. The Reynolds number based on the chord length and the inflow velocity is 101.

The motion of the foil is decided based on the equation of the motion:

$$I_o \frac{d^2\theta}{dt^2} = M_o \tag{7}$$

where M_o is the torque acting on the foil due to the viscous flow. To calculate the torque acting on the foil, the stress tensors are computed at neighboring fluid nodes of each Lagrangian control point. The stress tensor is extrapolated at the Lagrangian control point based on the distances from the neighboring fluid nodes to the local normal line passing the Lagrangian control point. The minimum gird spacing is

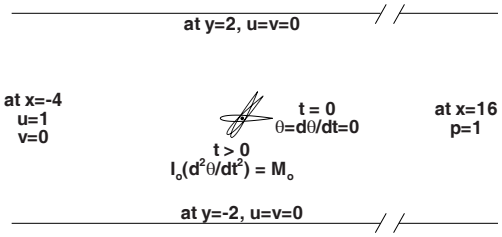

Fig. 4. Schematic drawing of the hinged NACA0012 in a channel. R_e =101.

0.005 near the foil. The artificial compressibility parameter β is set to 10.

In Fig. 5, the calculated time histories of the angle θ and the angular velocity $d\theta/dt$ of the foil are compared with those of Wan and Turek [14] and Glowinski [16]. The results are found to be stable after the foil starts to move, but the time interval to develop the initial motion and the direction of the movement vary irregularly according to tiny numerical parameter change. To compare the results without this irregularity, the time axis is shifted and the sign of the angle θ is converted for the other computations. It can be seen that good agreement is achieved for the mean deflection angles, the amplitudes of the oscillations and the periods of the motion. All computational results predict that the foil moves more slowly near the maximum deflection compared with the sinusoidal oscillation with a mean deflection.

In Fig. 6, the vorticity fields around the foil are shown at t =12, 13, 14 and 15. The angle of the foil reaches its local minimum between t =12 and 13 and increases until t =14. During this time interval, the fluids which pass the leading edge move upward. This upward motion severs the shear flow which passed the trailing edge and generates an isolated vorticity of clockwise rotation.

In Fig. 7, the contours of the velocity magnitude and pressure are shown near the trailing edge. The velocity varies continuously up to the body surface according to the velocity gradient in the boundary layer of the upper surface. The hybrid Cartesian/immersed boundary method based on the hybrid

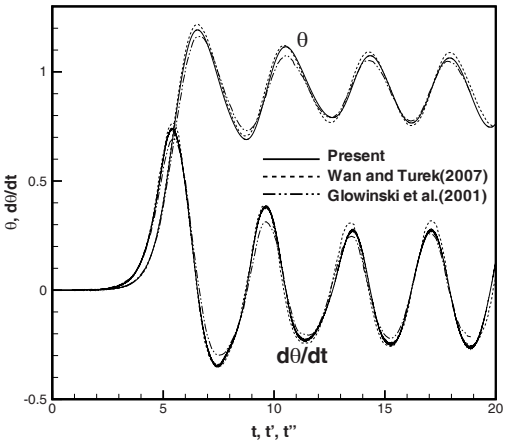

Fig. 5. Time histories of the angle and angular velocity of the hinged NACA0012 in a channel. Wan and Turek [14], $t' = t + 1.5$; Glowinski et al. [16], $t'' = t + 0.9$.

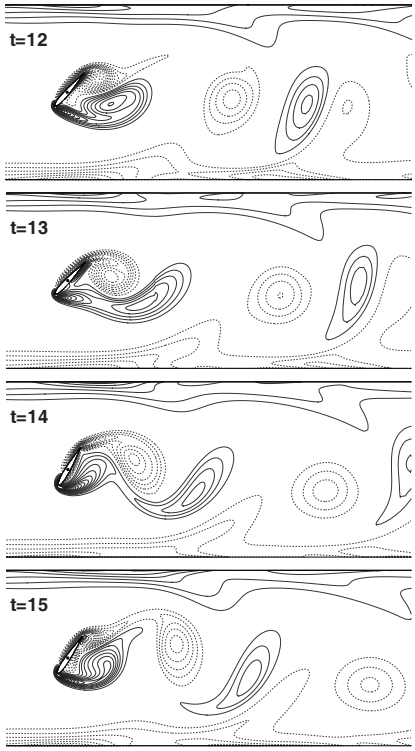

Fig. 6. Time evolution of the vorticity fields around the hinged NACA0012 in a channel. $-20 \leq \omega \leq 20$, $\Delta\omega$ =1.

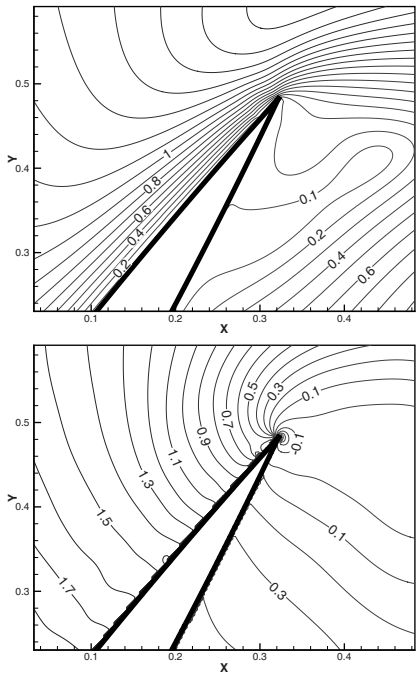

Fig. 7. Velocity magnitude and pressure contours near a trailing edge of the hinged NACA0012 in a channel at t =15.

staggered/non-staggered grid can resolve the pressure field smoothly near a sharp moving boundary without additional treatment [13]. The only presupposition for the computed flow field is that the reconstructed velocity vectors at the immersed boundary nodes are accurate. It implies that the grid should be fine enough to resolve the linear variation of the velocity along the local normal line near the body boundary.

4. Fluid-structure interaction of a moving flexible foil

In this section, the fluid-structure interaction of a moving flexible foil is simulated where the foil undergoes large amplitude dynamic deformation due to the fluid loading. Fig. 8 shows a schematic drawing of this example. The foil is a NACA0012 section and it oscillates in a fluid at rest. It is assumed that the foil is flexible from 0.2 chord to the trailing edge and the elastic deformation of the foil can be modeled based on the classical thin-plate mechanics [17, 18].

$$\rho_s b_s \frac{\partial^2 \eta}{\partial t^2} + d_s \frac{\partial \eta}{\partial t} + B_s \frac{\partial^4 \eta}{\partial \xi^4} = -\nabla q \tag{8}$$

where $\eta(\xi, t)$, ρ_s, b_s, d_s, B_s and $\nabla q(\xi, t)$ are, respectively, deformation, density of plate, thickness of plate, structural damping, flexural rigidity of plate and fluid loading distribution. In this study, the structural damping is ignored so that d_s =0. The Eq. (8) can be non-dimensionalized based on the chord length of the foil L, the density of fluid ρ and the characteristic velocity U.

$$\frac{\partial^2 \eta}{\partial t^2} + C_B \frac{\partial^4 \eta}{\partial \xi^4} = -C_\rho \nabla q \tag{9}$$

$$C_B = \frac{B_s}{\rho_s U^2 b_s L^2}, \quad C_\rho = \frac{\rho L}{\rho_s b_s} \tag{10}$$

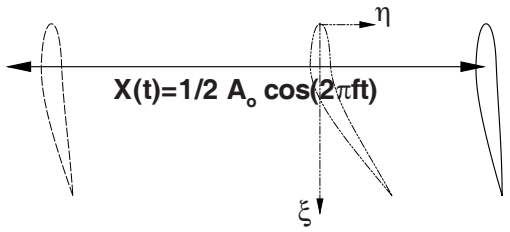

Fig. 8. Schematic drawing of the moving flexible foil. R_e=75.

The boundary conditions for a clamped end and a free end are given as follows.

$$\eta = \frac{\partial \eta}{\partial \xi} = 0 \quad \text{at} \quad \xi = 0.2 \tag{11}$$

$$\frac{\partial^2 \eta}{\partial \xi^2} = \frac{\partial^3 \eta}{\partial \xi^3} = 0 \quad \text{at} \quad \xi = 1 \tag{12}$$

To calculate the distribution of the plate deformation, the mean chord line is discretized. For every plate segment, the Lagrangian control points are selected to integrate the fluid loading acting on the given plate segment. Based on the estimated distribution of the fluid loading ∇q_j, the Eq. (9) is solved by using the finite difference method.

$$\frac{\eta_j^{n+1} - 2\eta_j^n + \eta_j^{n-1}}{\Delta t^2} + C_B \frac{\eta_{j+2}^n - 4\eta_{j+1}^n + 6\eta_j^n - 4\eta_{j-1}^n + \eta_{j-2}^n}{\Delta \xi^4} = -C_\rho (\nabla q)_j^n \tag{13}$$

Once the deformation of the mean chord line is computed at the new physical time step, the velocity distribution due to the deformation is estimated based on the time variation of the deformation. To provide the boundary conditions for the flow solver at the new physical time step, the position and velocity vectors at the Lagrangian control points are updated.

The selected physical parameters of this example are similar to those used by Eldredge [19] and Wang et al. [20] in order to simulate the insect flight based on the translational and rotational motion of the rigid elliptic wing. The rigid part of the foil undergoes the prescribed sinusoidal translational motion as follows:

$$X(t) = \frac{1}{2} A_o \cos(2\pi f t) \tag{14}$$

where the translational amplitude A_o is 2.8. The frequency f is given as $1/(\pi A_o)$ so that the maximum translational velocity is one. The Reynolds number, based on the maximum translational velocity and the chord length of the foil, is 75. The parameters C_B and C_ρ related to the flexibility and inertia of the plate, are 0.02 and 0.1, respectively.

To test the independency of the computed results on grids, three different-size grids are used. The minimum grid spacing for the fine, medium and

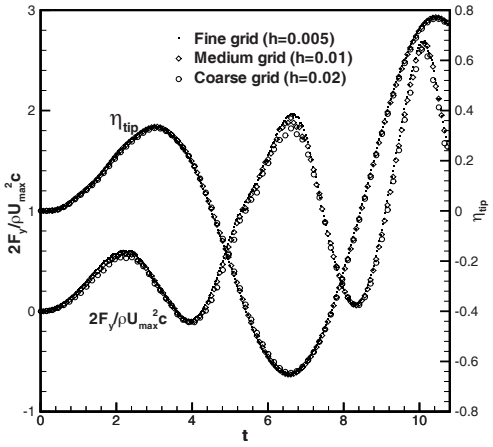

Fig. 9. Grid independency tests for computed time histories of the vertical force and the tip deflection.

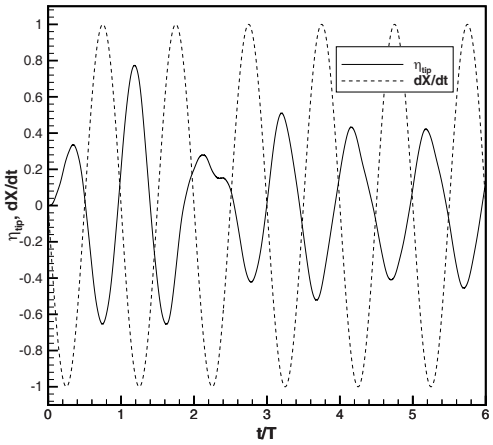

Fig. 10. Time histories of tip deflection and translational velocity of the moving flexible foil.

coarse grid is 0.005, 0.01 and 0.02, respectively. For the deformation calculation, the mean chord line is discretized by 20 elements. Even though the number of the structure elements was varied, there was virtually no effect on the computed results. As explained by Shin et al. [13], the response of the structure is dominated by the low-order eigenmode regardless of the rapid variations of the fluid loading in time and space due to the filtering effects of the structure itself.

Fig. 9 shows the variation in time histories of the computed vertical force F_y and the tip deflection η_{tip} according to the grid spacing. While there is slight variation in the computed force F_y, the computed tip deflection η_{tip} does not show notable deviation. Usually, it is more difficult to get rid of the grid dependency for the non-boundary conforming methods because of the additional treatments near the body boundary. For the hybrid Cartesian/immersed boundary method, it is crucial that the grid spacing should be fine enough to resolve the assumed velocity profile near the immersed boundary node. However, in this example, it is easier to get the converged solution for the hybrid Cartesian/immersed boundary method because of the low Reynolds number.

Fig. 10 shows the time histories of the tip deflection η_{tip} and the translational velocity. It is observed that the deflection reaches its local maximum somewhat prior to the moment when the rigid part moves with the maximum velocity. One of the reasons which causes this time gap is the effect of the added mass. During the translational velocity of the foil increases, the acceleration of the foil induces the decreasing force in the opposite direction of the movement. As combined effects of the velocity and acceleration of the foil, the fluid loading reaches its local maximum before the foil moves with its maximum velocity.

Fig. 11 shows the time evolution of the vorticity and pressure fields around the moving flexible foil. At t =5.0 T, the translational velocity of the foil is zero, but the acceleration of the foil and the local velocity and acceleration due to the deformation induce the significant pressure modification near the foil. As the translational velocity increases from t =5 T to t =5.2 T, the tip trails due to the fluid loading. During this time interval, the fluid pushed by the foil near the leading edge tends to move downward because the trailing edge evacuates due to the deformation. This downward flow contributes to the upward vertical force as shown later. As the translational velocity decreases, the elastic force of the plate restores the original configuration. At t =5.4 T, the deformation is significantly decreased already. At t =5.6 T, the foil moves in the opposite direction and the deflection is converted.

In Figs. 12 and 13, the contours of vorticity and vertical velocity are compared for the cases of flexible and rigid foils. As mentioned previously, the deflection of the tip causes the downward flow and the vortices shed from the foil align with the vertical center line for the flexible foil. For the vertical velocity, downward velocity dominates the central area below the foil.

In Fig. 14, the time histories of the vertical and horizontal force acting on the moving flexible foil are compared with those acting on the rigid foil. For the rigid foil, the vertical force reflects the effects of the

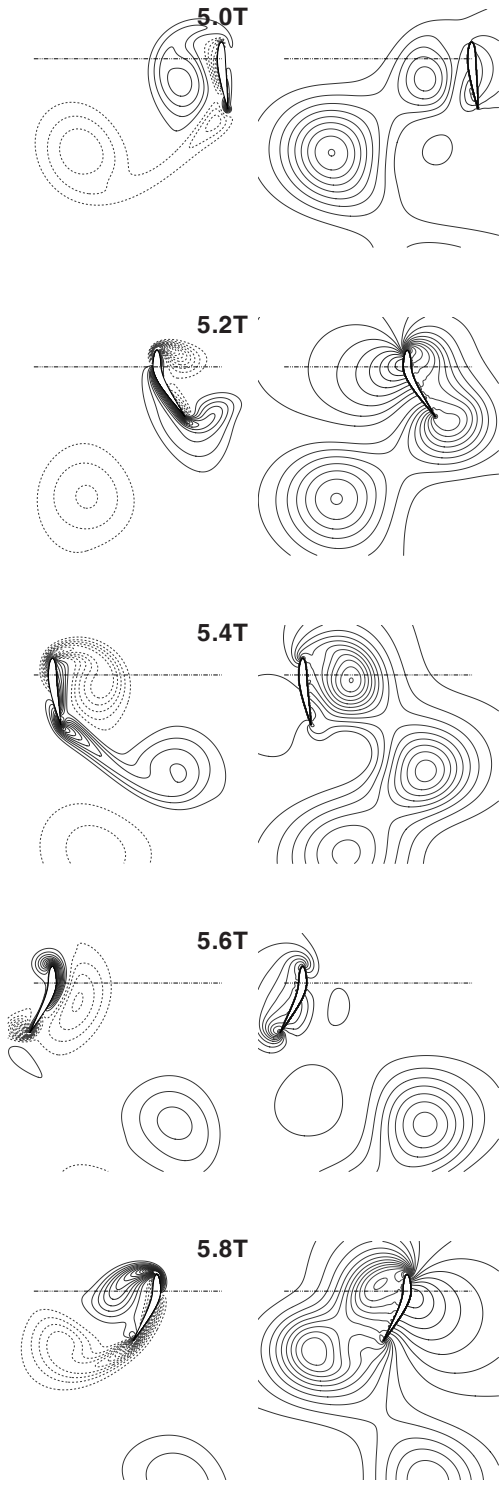

Fig. 11. Time evolution of vorticity (left) and pressure (right) fields around the moving flexible foil. $-20 \leq \omega \leq 20$, $\Delta\omega = 1$; $-0.5 \leq p \leq 2$, $\Delta p = 0.1$.

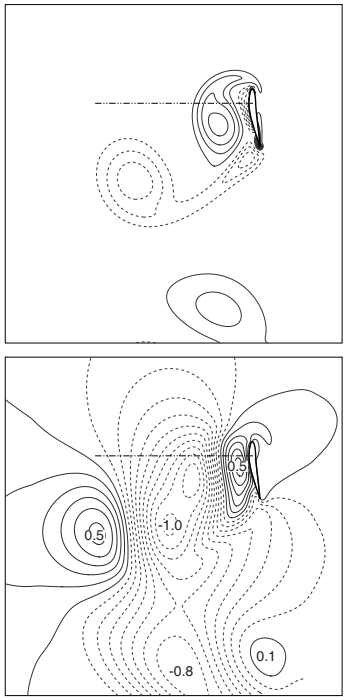

Fig. 12. Contours of vorticity and vertical velocity around the moving flexible foil at $t = 6T$. $-20 \leq \omega \leq 20$, $\Delta\omega = 1$; $-1 \leq v \leq 0.5$, $\Delta v = 0.1$.

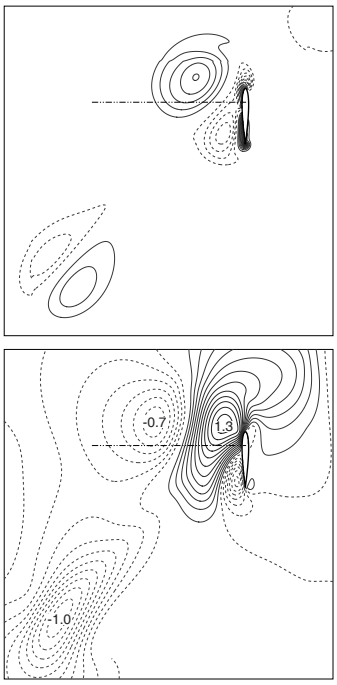

Fig. 13. Contours of vorticity and vertical velocity around the moving rigid foil at $t = 6T$. $-20 \leq \omega \leq 20$, $\Delta\omega = 1$; $-1 \leq v \leq 1.3$, $\Delta v = 0.1$.

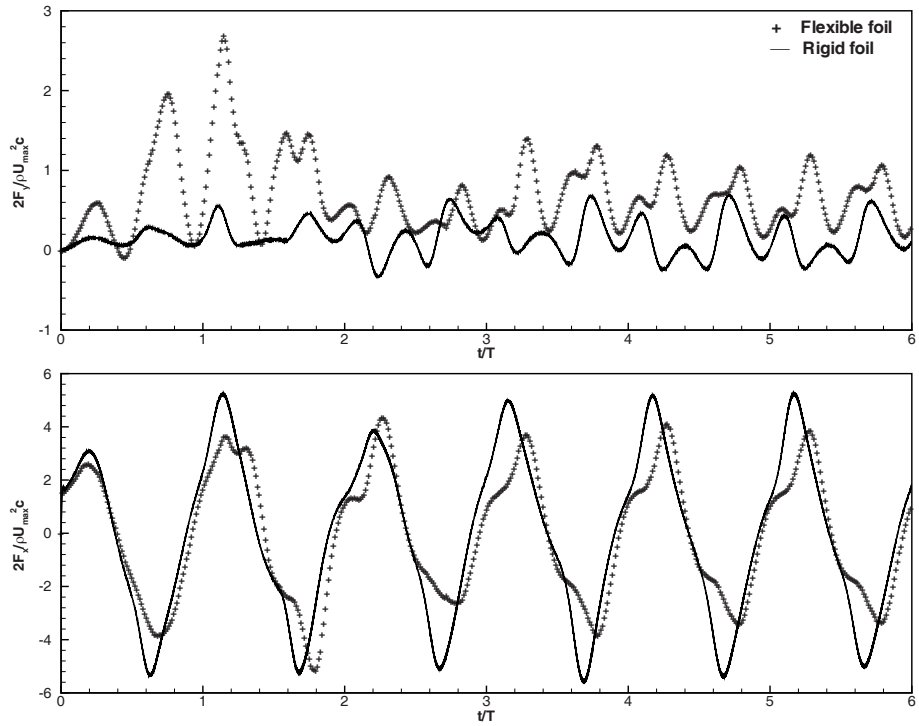

Fig. 14. Effects of flexibility of foil on the vertical and horizontal forces acting on the moving foils.

different configurations between the leading and trailing edges. As the boundary layer near the foil develops, the time average of the vertical force gets close to zero for the rigid foil. Although the time average of the vertical force decreases also for the flexible foil, a significant upward force persists for the flexible foil due to the downward motion of the fluid caused by the alternating tip deflection. This upward force of the flexible foil can be explained also based on the instantaneous configuration of the deforming foil. The tail of the foil is pushed from higher pressure side to lower pressure side. As a result of the instantaneous deformation, the lower surface of the tail contacts with the higher pressure fluid and the lower pressure pulls the tail upward. The flexibility of the foil reduces the magnitude of the horizontal force. The difference in the horizontal force is more apparent near the peak where the deflection of the foil is more significant.

5. Conclusions

A hybrid Cartesian/immersed boundary method has been applied to simulate the fluid-structure interaction of the moving flexible foil. A new procedure has been suggested to identify each node as a fluid, solid or immersed boundary node based on edges crossing the boundary. The present criterion provides appropriate boundary conditions for the flow solver based on the hybrid staggered/non-staggered grid method, and it can handle a zero-thickness body without any difficulty.

The developed code has been applied to simulate the rotational motion of an NACA0012 in a channel of a viscous fluid, and the results have been compared with other computations. Good agreement has been achieved for the calculated period, mean deflection angle and amplitude of the oscillation. It has been also observed that the hybrid Cartesian/immersed boundary method provides a smooth pressure field near a moving sharp boundary without any additional treatment.

The fluid-structure interaction of the moving flexible foil has been simulated. For this low Reynolds number, the grid independency has been established with moderate grid requirement. It has been observed that the response of the structure is smoother than the variation of the fluid loading due to the filtering effects of the structure. The moving flexible foil has been shown to generate larger vertical force than the

corresponding rigid foil, and the vertical force has contributed to the downward fluid jet due to the alternating tip deflection. The downward fluid jet has been also supported by the comparisons of the vorticity and vertical velocity contours with those of the rigid foil.

Acknowledgments

This work was supported by the Underwater Vehicle Research Center (UVRC, SM-42), Korea.

References

[1] M. M. Murray and L. E. Howle, Spring stiffness influence on an oscillating propulsor, *Journal of Fluids and Structures*, 17 (7) (2003) 915-926.

[2] J. M. Miao and M. H. Ho, Effect of flexure on aerodynamic propulsive efficiency of flapping flexible airfoil, *Journal of Fluids and Structures*, 22 (3) (2006) 401-419.

[3] A. Masud, M. Bhanabhagvanwala and R. A. Khurram, An adaptive mesh rezoning scheme for moving boundary flows and fluid-structure interaction, *Computers & Fluids*, 36 (1) (2007) 77-91.

[4] K. Namkoong, H. G. Choi and J. Y. Yoo, Computation of dynamic fluid-structure interaction in two-dimensional laminar flows using combined formulation, *Journal of Fluids and Structures*, 20 (1) (2005) 51-59.

[5] B. E. Griffith, R. D. Hornung, D. M. McQueen and C. S. Peskin, An adaptive, formally second order accurate version of the immersed boundary method, *Journal of Computational Physics.*, 223 (1) (2007) 10-49.

[6] D. Kim and H. Choi, Immersed boundary method for flow around an arbitrarily moving body, *Journal of Computational Physics*, 212 (2) (2006) 662-680.

[7] D. Kim and H. Choi, Two-dimensional mechanism of hovering flight by single flapping wing, *Journal of Mechanical Science and Technology*, 21 (1) (2007) 207-221.

[8] M. L. Linnick and H. F. Fasel, A high-order immersed interface method for simulating unsteady incompressible flows on irregular domains, *Journal of Computational Physics*, 204 (1) (2005) 157-192.

[9] H. S. Udaykumar, R. Mittal, P. Rampunggoon and A. Khanna, A., A sharp interface Cartesian grid method for simulating flows with complex moving boundaries, *Journal of Computational Physics*, 174 (1) (2001) 345-380.

[10] A. Gilmanov, F. Sotiropoulos and E. Balaras, A general reconstruction algorithm for simulating flows with complex 3D immersed boundaries on Cartesian grids, *Journal of Computational Physics*, 191 (2) (2003) 660-669.

[11] A. Gilmanov and F. Sotiropoulos, A hybrid Cartesian/immersed boundary method for simulating flows with 3D, geometrically complex, moving bodies, *Journal of Computational Physics*, 207 (2) (2005) 457-492.

[12] L. Ge and F. Sotiropoulos, A numerical method for solving the 3D unsteady incompressible Navier-Stokes equations in curvilinear domains with complex immersed boundaries, *Journal of Computational Physics*, Vol. 225 (2) (2007) 1782-1809.

[13] S. Shin, S. Y. Bae, I. C. Kim, Y. J. Kim and J. S. Goo, Computations of flow over a flexible plate using the hybrid Cartesian/immersed boundary method, *International Journal for Numerical Methods in Fluids*, 55 (3) (2007) 263-282.

[14] D. Wan and S. Turek, Fictitious boundary and moving mesh methods for the numerical simulation of rigid particulate flows, *Journal of Computational Physics*, 222 (1) (2007) 28-56.

[15] R. Glowinski, T. W. Pan, T. I. Helsa, D. D. Joseph and J. Periaux, A distributed Lagrange multiplier/fictitious domain method for flows around moving rigid bodies: Application to particulate flow, *International Journal for Numerical Methods in Fluids*, 30 (8) (1999) 1043-1066.

[16] R. Glowinski, T. W. Pan, T. I. Helsa, D. D. Joseph and J. Periaux, A fictitious domain approach to the direct numerical simulation of incompressible viscous flow past moving rigid bodies: Application to particulate flow, *Journal of Computational Physics*, 169 (2) (2001) 363-426.

[17] T. S. Balint and A. D. Lucey, Instability of a cantilevered flexible plate in viscous channel flow, *Journal of Fluids and Structures*, 20 (7) (2005) 893-912.

[18] I. H. Shames and C. L. Dym, *Energy and Finite Element Methods in Structural Mechanics*, Taylor & Francis, Bristol, (1985).

[19] J. D. Eldredge, Numerical simulation of the fluid dynamics of 2D rigid body motion with the vortex particle method, *Journal of Computational Physics*, 221 (2) (2007) 626-648.

[20] Z. J. Wang, J. M. Birch and M. H. Dickinson, Unsteady forces and flows in low Reynolds number hovering flight: Two-dimensional computations vs

robotic wing experiments, *Journal of Experimental Biology*, 207 (3) (2004) 449-460.

Sangmook Shin received his B.S. and M.S. degrees in Naval Architecture from Seoul National University, Korea in 1989 and 1991, respectively. He received his Ph.D. degree in Aerospace Engineering from Virginia Tech, USA in 2001. He is currently an Assistant Professor at Department of Naval Architecture and Marine Systems Engineering at Pukyong National University in Busan, Korea. His research interests include fluid-structure interaction, unstructured grid method, internal wave, and two-phase flow.

Hyoung Tae Kim received the B.S. and M.S. degrees in Naval Architecture from Seoul National University in 1979 and 1981, respectively and the Ph.D. degree in Mechanical Engineering from University of Iowa, U.S.A. in 1989. Dr. Kim is currently a Professor at the Department of Naval Architecture & Ocean Engineering at Chungnam National University, Korea. His research interests are in the area of Ship Hydrodynamics, CFD calculations of turbulent flows around ships and propellers, and human-powered and solar boat design.